Magneto-Inductive Communication for Subsurface Exploration of Europa

Joshua Wornell,* **Michael Cheng,†** **and Dariush Divsalar‡**

ABSTRACT. — Exploration of ocean worlds such as Europa offers potentially important and unique scientific findings. To explore these oceans, technology suitable for the distinct environments must be developed. Europa's subsurface ocean lies under a large sheet of ice that could be tens of kilometers thick. This uncommon thick ice barrier makes communication to a subsurface probe difficult. In this work, we investigate a magneto-inductive (MI) communication system that has the potential to operate in environments where traditional radio frequency (RF) communication would struggle, such as liquid waters, slush, or higher-temperature ice.

I. Introduction

Subsurface exploration of ocean worlds such as Europa could offer unique scientific discoveries and data. In the case of Europa, its interior ocean is hidden beneath a thick layer of ice kilometers to tens of kilometers thick. This icy surface layer poses a unique challenge for communication to and from a subsurface probe. For this purpose, we propose a hybrid MI and RF system to penetrate the icy medium. For the data-intensive forward (probe-to-lander) link, we envision an MI-to-RF relay that will use MI closest to the ocean through warm slushy ice because RF communication is difficult in this region. Once the ice shell turns into colder and harder ice, data will be relayed via RF the rest of the way up to the surface. This way, each MI and RF link would be used at its respective strengths as seen in Figure 1.

Salty water and briny ice often are difficult mediums for wireless communications

*Undergraduate Intern Massachusetts Institute of Technology, Cambridge, Massachusetts.

†Communications Ground Systems Section.

‡Communications Architectures and Research Section.

The research described in this publication was carried out by the Jet Propulsion Laboratory, California Institute of Technology, under a contract with the National Aeronautics and Space Administration.

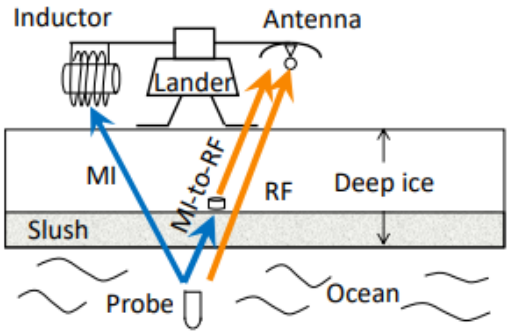

Figure 1. RF, MI, and Hybrid RF and MI System Diagram

because their high electrical conductivity cause most signals to attenuate at faster rates compared to vacuum. Many traditional communication systems that work very well in air fail to provide the same flexibility and benefits underwater. Candidate through-ice communication methods are RF, acoustic, and an optical tether. RF communication typically operates at high frequencies, and at these frequencies the signal attenuation underwater is severe. Extremely low-frequency systems, operating around 3 Hz to 30 Hz, and very low-frequency systems, operating around 300 Hz to 3 kHz, are able to penetrate water to some depths. However, the size of the antenna must be very large due to the long wavelengths and can only communicate at very low data rates. Acoustic signals propagate well in water at low frequencies and can penetrate relatively large distances, but the acoustic transducers require a tight seal with ice to minimize loss, and the acoustic signal suffers from high propagation delays and seismic background interference. Wired fiber-optic cables, while providing the highest data rates and communication distances assuming a long enough cable, are at risk of shear and tear due to seismic activities of the ice shell. Moreover, armoring kilometers of cables to prevent breakage would require a large amount of weight.

There has been work and published research on MI communications experiments in the past in which different experiments used different coil configurations, transmit powers, and respective sensitivities to achieve their max distances. These prior works have achieved distances from 3 m all the way to 400 m. These works and their respective distances are shown in Table 1.

Table 1. Prior work done on underwater MI communications.

Experiment Name	ROA-RCB: Fresh Sea Water [1]	SEA-TEL: Surface to Diver [2]	M2I: Underwater and Underground [3]	CSS/MISL: Air Ocean Water [4]
Distance	3 m	30 m	50 m	250–400 m

We, however, aim to use a highly sensitive magnetometer with a sensitivity in the range of $100\frac{fT}{\sqrt{Hz}}$ in the 1–100 kHz region as a receiver coil. Due to resource

limitations on the ocean probe, we aim to achieve a data rate in the 10–100 bits-per-second range. To have a low-complexity implementation of the receiver, non-coherent demodulation is selected. Thus we are considering simple modulation schemes, namely on-off keying (OOK) and frequency shift keying (FSK). The cryobot will likely be resource constrained and does not require a high data rate. We are interested in schemes that are straightforward to implement and not computationally intensive. OOK also allows us to operate at a single resonance frequency where the magnetic field response is at its highest. This paper will discuss the application of OOK modulation with a low-density parity check (LDPC) code (a forward error correction (FEC) code) at low data rate to an MI communication link.

II. System Hardware and Testing Setup

A. The Transmitter and Receiver Hardware

In the MI prototype system that was used for this work, the transmitter setup was a commercial-off-the-shelf (COTS) copper MI coil with an inductance of 95.74 mH, capacitance of 300 pF, and a DC resistance of 18.5 ohms. The coil has an inner radius of 10.06 cm, an outer radius of 11.37 cm, a width of 1.6 cm, 500 turns, and a wire diameter of 0.64 mm. A picture of the coil is given in Figure 2. The dimension of this COTS coil is compatible with the size of a concept cryobot. An identical MI coil is used as the receiver for the system. During testing, a battery was connected to an arbitrary waveform generator (AWG), which is then connected to a waveform amplifier. Since we are driving the coil with an AC current, the coil impedance Z is a function of the carrier frequency $Z = 2\pi f L$, where L is the inductance of the coil. Our COTS coil has a high inductance and, therefore, a high impedance at high frequency f. To reduce the impedance and allow more current into the coil, we put a resonance capacitor in series with the transmitter coil and another one in parallel with the receiver coil. The capacitor value is calculated as $C = \frac{1}{L(2\pi f)^2}$. For an AC with $f = 1$ kHz, the resonance capacitor is 0.22 μF. The experimental MI communication link setup is shown in Figure 3.

Figure 2. PASCO 500-turn copper coil with an outer diameter of almost 23 cm.

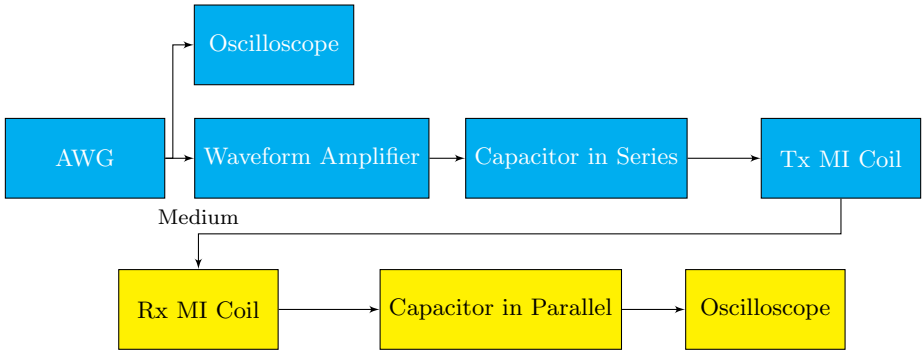

Figure 3. Block diagram showing test setup for experiments. Transmitter (Tx) blocks are cyan, and receiver (Rx) blocks are yellow.

B. Test Setup and Procedures

For testing of the MI system prototype, the coils were brought out to a sufficiently long-range area, often a parking lot or other flat paved surface, and set to a specified distance apart. First, a background noise measurement and a sinusoidal tone measurement were made for both 1 kHz and 10 kHz. Next, a specified psuedorandom binary number sequence was transmitted at both 1 kHz and 10 kHz. The number sequence was used for all recordings and used for calculating bit error rate (BER) after demodulation of the waveform. This process was repeated at different distances until the received signal had attenuated enough that the signal was no longer observable on the oscilloscope. All tests were recorded on an oscilloscope, and the data was saved on a USB drive. Additionally, tests following the same procedure were conducted in a pool underwater.

III. Non-Coherent On-Off Keying Analysis

A. Error Rate Analysis

The system utilized in the testing and analysis of the MI system uses OOK modulation with random phase. For this communication system, we assume a random phase θ that is uniformly distributed with probability density function (pdf) $p(\theta) = \frac{1}{2\pi}$ for $0 \leq \theta \leq 2\pi$. For simplicity and low complexity, the receiver does not track this phase therefore it can be classified as non-coherent reception. For non-coherent OOK, suppose that the received observation for data bit 1 is

$$r(t) = \sqrt{2P}\sin(2\pi f t + \theta) + n(t), \tag{1}$$

where $n(t)$ is the received noise, P is the received peak power, and f is the frequency. For data bit 0, the received observation is

$$r(t) = 0 + n(t). \tag{2}$$

Using a maximum likelihood decision rule, the average error rate for our system will

be theoretically represented as

$$P_e = \frac{1}{2}\left(1 - Q_1\left(\sqrt{\frac{2E}{N_0}}, \frac{1}{2}\sqrt{\frac{2E}{N_0}+8}\right)\right) + \frac{1}{2}e^{-\frac{1}{4}\frac{E}{N_0}-1}, \tag{3}$$

where E is the peak symbol energy and N_0 is the one-sided noise power spectral density. If we define $\bar{E}$ to be the average energy per symbol, then $\bar{E} = \frac{E}{2}$, and we get the following set of equations:

$$P_e = \frac{1}{2}\left(1 - Q_1\left(\sqrt{\frac{4\bar{E}}{N_0}}, \frac{1}{2}\sqrt{\frac{4\bar{E}}{N_0}+8}\right)\right) + \frac{1}{2}e^{-\frac{1}{4}\frac{2\bar{E}}{N_0}-1}, \tag{4}$$

where $Q_1\left(\sqrt{\frac{4\bar{E}}{N_0}}, \zeta\right)$ is the Marcum Q function with threshold $\zeta = \frac{1}{2}\sqrt{\frac{4\bar{E}}{N_0}+8}$. The full derivation, along with other approximations of this error rate, can be found in the Appendix. In Section IV, this theoretical error rate will be compared with measured error rates using our prototype system. The signal-to-noise ratio for one-dimensional modulation usually is defined as $SNR = \frac{2\bar{E}}{N_0}$.

B. Channel Coding Analysis

In this section, we consider a channel coded non-coherent OOK system. We used the rate 1/2 LDPC code (2048, 1024) in the Consultative Committee for Space Data System (CCSDS) standard as an example. For simulations, we used MATLAB Simulink models. For our system setup in Simulink, we considered an equivalent baseband model as in the Appendix. The received observations in Equations (19) and (20) can be normalized by $\sqrt{E}$ and can be represented by complex received samples

$$H_1 : Y = e^{j\phi} + N \tag{5}$$

and

$$H_0 : Y = N, \tag{6}$$

where the N is a complex zero mean Gaussian noise with variance $\sigma^2 = \frac{1}{2E/N_0}$ per dimension. For channel transmission rate of $\frac{1}{T}$, the $E = PT$ corresponds to peak energy per symbol duration T, where P is the peak received power. For the above observation equations, the magnitude of observations now is $Z = \frac{R}{\sqrt{E}}$, where R is defined in the Appendix. The probability density functions of R under two hypotheses are given in equations (26) and (27), allowing us to compute the corresponding pdf of Z. Replacing $\frac{2E}{N_0} = \frac{1}{\sigma^2}$ in the pdf for Z, we obtain

$$H_1 : f_1(z) = \frac{1}{\sigma^2} z e^{-\frac{1}{2\sigma^2}\left(z^2+1\right)} I_0\left(\frac{z}{\sigma^2}\right) \tag{7}$$

and

$$H_0 : f_0(z) = \frac{1}{\sigma^2} z e^{-\frac{1}{\sigma^2}z^2}. \tag{8}$$

The log likelihood ratio (LLR) to be provided to the decoder is

$$LLR(z) = \ln \frac{f_1(z)}{f_0(z)} = -\frac{1}{2\sigma^2} + \ln I_0\left(\frac{z}{\sigma^2}\right). \tag{9}$$

By setting LLR = 0, we can compute a decision threshold for declaring each bit to be a 0 or a 1 in the uncoded system. For large x, we have

$$\ln I_0(x) \approx x - \frac{1}{2}\ln(2\pi x). \tag{10}$$

Therefore, the approximate LLR is

$$LLR(z) = -\frac{1}{2\sigma^2} + \frac{z}{\sigma^2} - \frac{1}{2}\ln\left(2\pi\frac{z}{\sigma^2}\right). \tag{11}$$

If we don't want to use the logarithmic function for computation of approximate LLR, we propose the following suboptimal approximation for the LLR based to threshold $\zeta_2^{'}$:

$$LLR(z) = \frac{1}{\sigma^2}\left(z - \zeta_2^{'}\right), \tag{12}$$

where $\zeta_2^{'} = \frac{1}{2} + 2\sigma^2$.

This calculation mimics that of η_2 in the Appendix. Since here we normalized the R by $\sqrt{E}$, the threshold is approximately $\zeta_2^{'} = \frac{1}{2}\sqrt{1+8\sigma^2}$. For a small value of σ^2, $\sqrt{1+8\sigma^2} \approx \left(1+4\sigma^2\right)$. In fact, $\zeta_2^{'} = \frac{1}{2} + 2\sigma^2$ is simpler and seems to be a better approximation for threshold.

The Simulink system block diagram is shown in Figure 4. In this figure, "AWGN" stands for the"Additive White Gaussian Noise". The demodulator using the

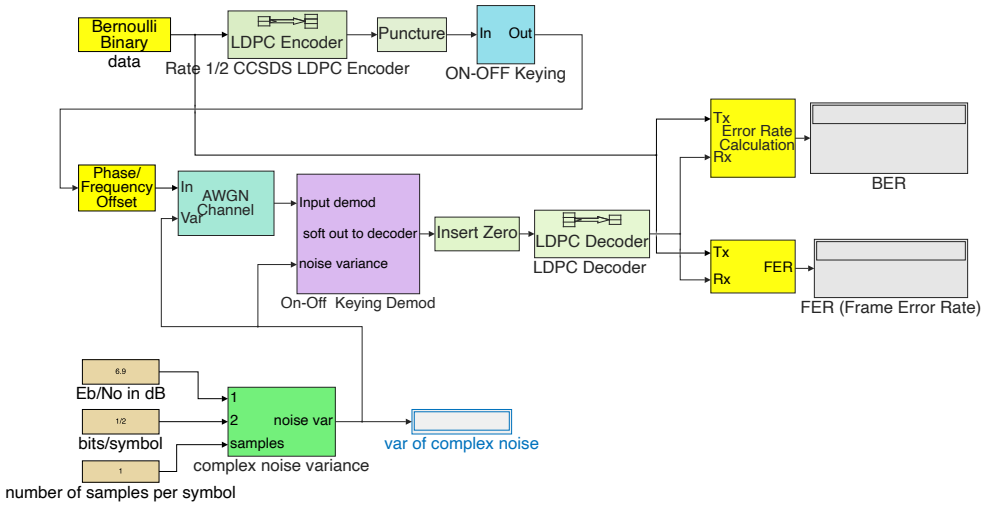

Figure 4. Coded system block diagram in Simulink.

approximate LLR is shown in Figure 5. The frame error rate (FER) results using the approximate LLR are shown in Figure 6. We also simulated the system in Figure 4

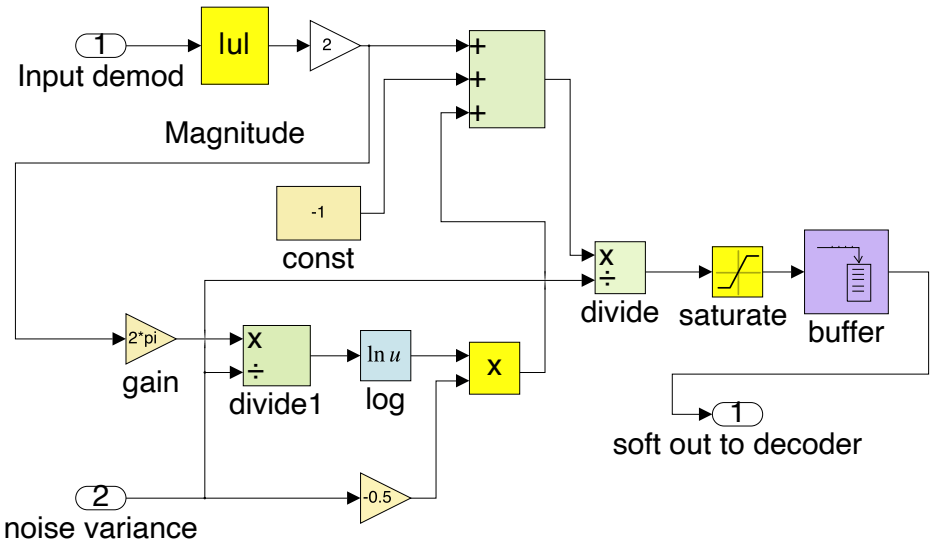

Figure 5. Demodulator with approximate LLR for coded non-coherent OOK.

using both the true value of LLR and suboptimal approximation for LLR given by Equation (12). For the suboptimal LLR, the demodulator is shown in Figure 7. In this figure, an alternative receiver for the uncoded system is also shown. The FER simulations using our approximation for the LLR are very close to the FER simulations for the exact value of the LLR, to within less than 0.05 dB. Performance simulations using the suboptimal LLR are within 0.1 dB compared to the FER using the exact LLR.

IV. Simulations and Experimental Results

In this section, we look at experimental results obtained from tests using the setup from Section II. The MI prototype system was tested at a range of distances between 1–30 m and at two different frequencies, 1 kHz and 10 kHz. The tests were also conducted in different locations on separate days, and the resulting noise power levels varied significantly. Most of the tests were conducted in parking lots where the coils were placed on the ground. Tests were also run inside a swimming pool, but due to the high signal attenuation through pool water and the fact that we were without a waveform amplifier for the pool test, the SNR was significantly lower at long distances, and communication was only achieved at a distance of approximately 50 cm. Magnetic field attenuation measured in our tests followed the Biot-Savart Law [5] and degraded as a function of $\frac{1}{d^3}$ from the source. Figure 8 shows our measured tone amplitude compared to a $\frac{1}{d^3}$ slope.

What limited our system performance in the field was the unexpected noise from our power source. A snapshot of the received test signal in both frequency domain and

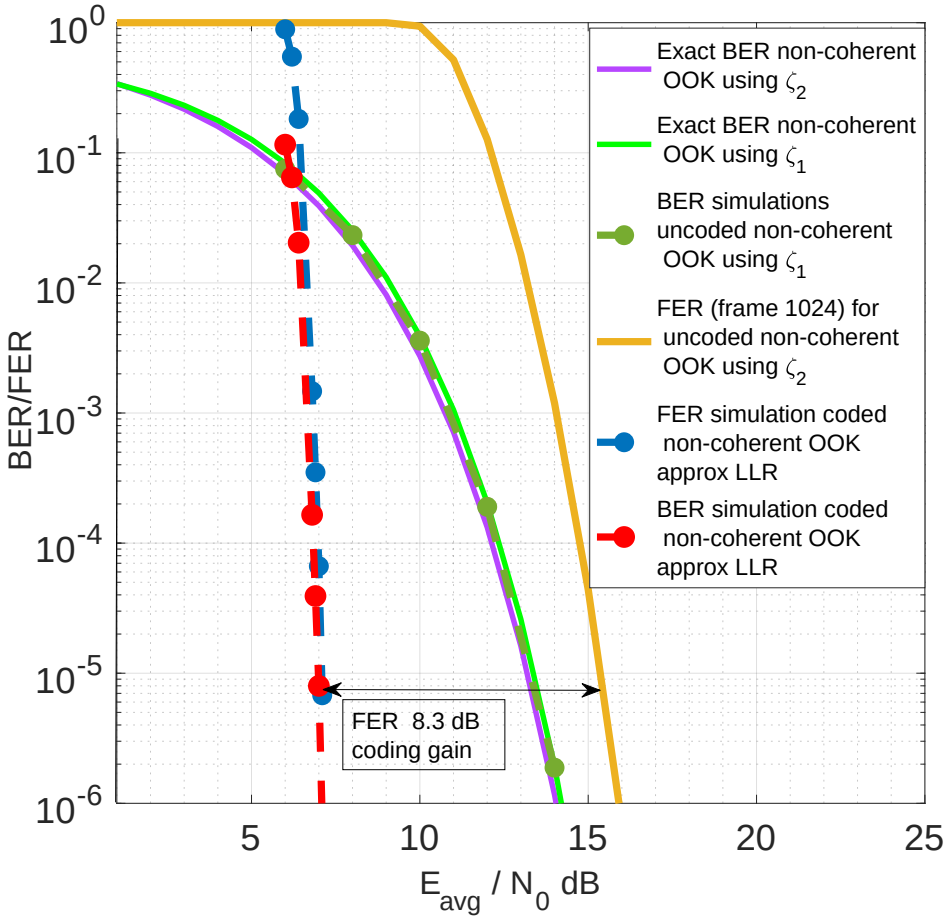

Figure 6. Performance of LDPC code with non-coherent OOK.

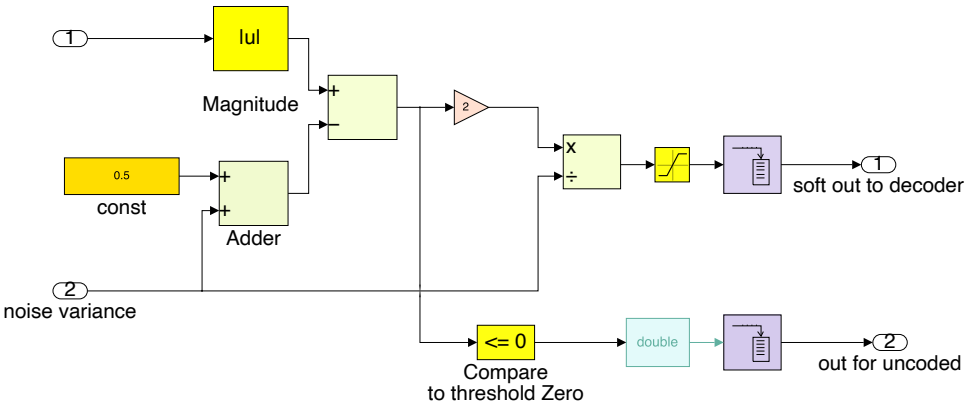

Figure 7. Demodulator with suboptimal LLR for coded non-coherent OOK.

time domain is shown in Figure 9. When we powered our system in field testing using COTS camping batteries at the transmitter and at the receiver, the receiver coil picked up DC-to-AC inverter noise generated by the batteries. The inverter noise manifested itself as spikes in the time series as seen in Figure 9. In the frequency domain, the inverter noise appeared as harmonic peaks spaced 60 Hz apart. If the data rate were higher than 10 bps, the 60 Hz harmonic noise would leak into the data and affect communication performance.

Figure 10 and Table 2 show the results for MI OOK communication using a 1 kHz carrier. The received signals were demodulated following the process depicted in Figure 11 and bit-error-rates (BERs) were computed. The derivation for the theoretical curve can be found in Section III. The arrows along the x axis in Figure 10 identify the measured points where the BERs were zero. Our measured BERs were lower than the theoretical curve, this can be attributed to having only a small amount of recorded data (about a few thousand bits for each data point due to the low data rate). For the West parking lot test, we achieved a BER of 0 at a distance of 20 m, and a BER of 12% at a distance of 30 m. At 20m we measured about 10 dB SNR, and at 30 m we measured about 1.3 dB SNR. Assuming the noise power is constant between the measurements, the signal power dropped close to 10 dB between the 2 distances and this result agrees with the Biot-Savart Law. That is, the signal power for MI attenuates as a function of $\frac{1}{d^6}$, so if the distance is 1.5$\times$ longer, we would expect the SNR to reduce by about 10 dB if the noise power stays constant. Moreover, the measured uncoded BER for noncoherent OOK at 30 m is close to the theoretical curve at 0.12 as seen in Figure 10.

Figure 12 and Table 3 show the result for 10 kHz. At this frequency, we encountered a BER of 10^{-2} at 10 m likely because we were not able to drive the 500-turn COTS coil with a significant amount of electrical current due to the higher impedance at a higher frequency compared to 1 kHz.

Table 2. 1 kHz carrier test results. Data rate was 10 bps. We blew the waveform amplifier fuse at the start of the Caltech pool test so results were without transmitter amplification for that day.

Location	Amp	medium	dist (m)	Frequency (kHz)	SNR (dB)	Average BER
Caltech Pool	No	Air	1	1.088	36.94	0
		Air	2	1.088	19.14	0
		Air	3	1.088	10.34	0
		Water	0.5	1.088	24.97	0
West parking lot	Yes	Air	10	1.097	19.14	0
		Air	20	1.097	10.34	0
		Air	30	1.097	1.31	.121
East parking lot	Yes	Air	5	1.093	19.99	0
		Air	10	1.093	6.88	0

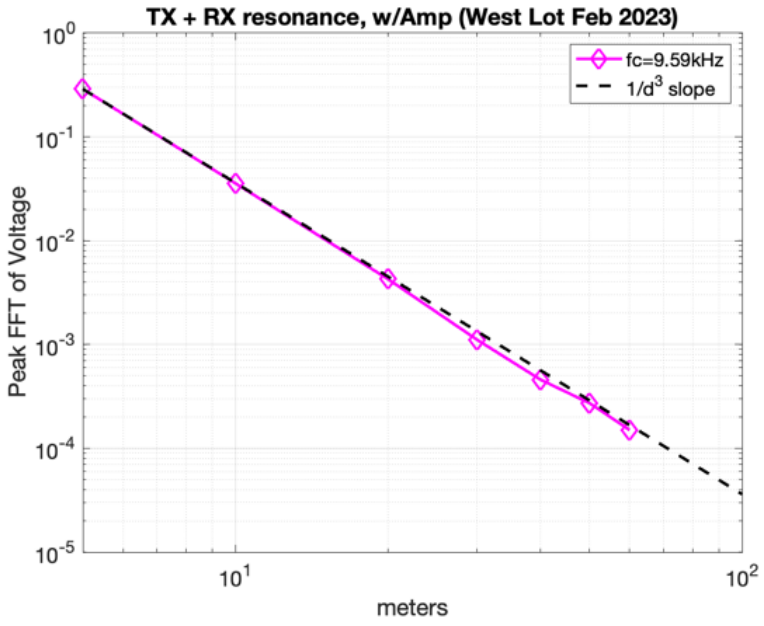

Figure 8. Tone amplitude over distance at 10 kHz. Data collected at a parking lot.

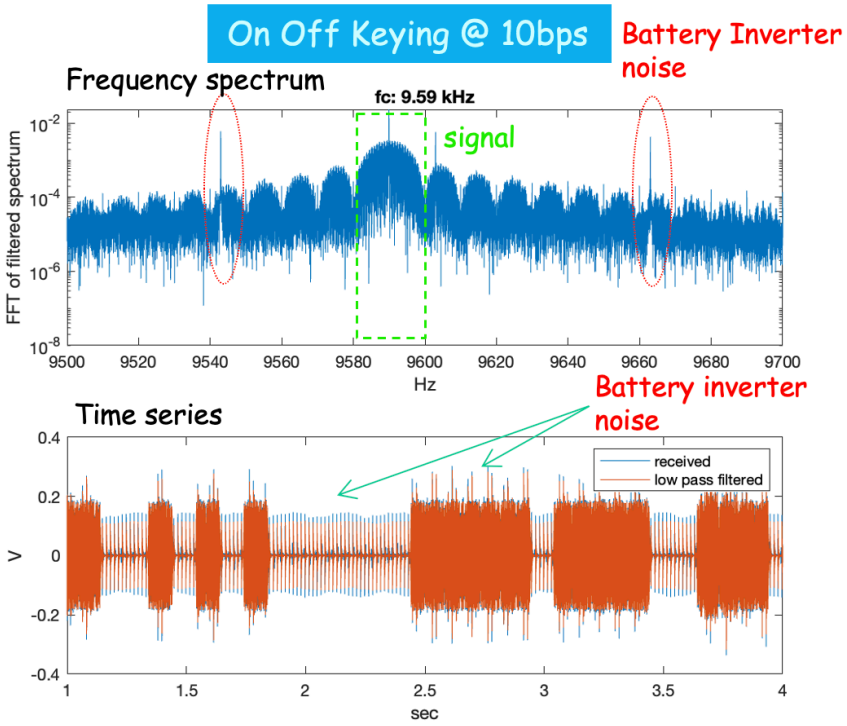

Figure 9. Frequency and time domain of received signal. Distance was 5 m, and data rate was 10 bps. Data collected at a parking lot.

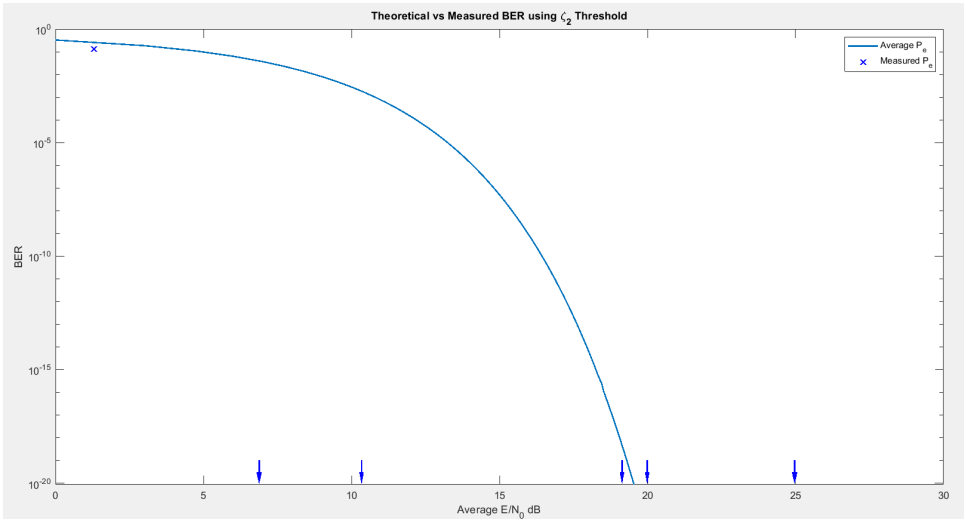

Figure 10. 1 kHz carrier BER results from Table 2 compared against theoretical BER. The arrows along the x axis identify the measured points in field testing where the BERs were zero. Due to the low data rate, we were not able to collect enough points in the field to trace the curve.

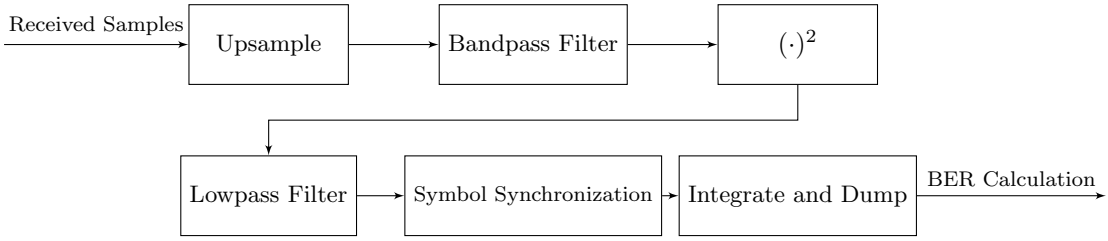

Figure 11. Block diagram showing method used to demodulate the received OOK signal.

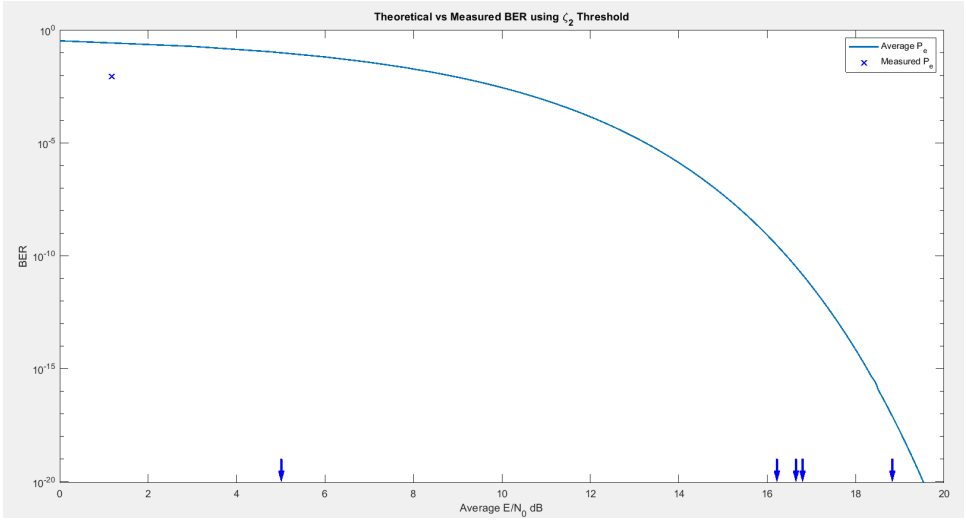

Figure 12. 10 kHz carrier BER results from Table 3 compared against theoretical BER. The arrows along the x axis identify the measured points in field testing where the BERs were zero. Due to the low data rate, we were not able to collect enough points in the field to trace the curve.

Table 3. 10 kHz carrier field test results. Data rate was 10 bps.

Location	Amp	Medium	dist. (m)	Frequency (kHz)	SNR (dB)	Average BER
West parking lot	Yes	Air	10	9.59	1.17	.00886
		Air	8	9.59	5.01	0
		Air	5	9.59	18.83	0
		Air	5	9.59	16.22	0
		Air	5	9.59	16.80	0
		Air	5	9.59	16.65	0

V. Concluding Remarks

We have presented in this paper an MI communication system for subsurface exploration of Europa. We derived the theoretical BER performance of a non-coherent OOK system both with and without the use of a forward error correcting channel code. The derived BER curve will be useful as we continue to test different MI communication systems in the field. The MI system under test was able to close a link with a positive SNR and the use of channel code will allow us to extend the achievable communication distance. From the presented simulations, using the rate 1/2 CCSDS LDPC (2048, 1024) channel code, we have shown roughly 8.3 dB of coding gain between a coded and an uncoded system at a FER of 10^{-6}.

This paper examined a specific pair of transmitter and receiver coils, but a similar system with a more sensitive receiver coil and a stronger transmitter is being tested and will extend the effective communication range even more. The new receiver coil is based on the Plasma Wave Subsystem of Galileo and has a sensitivity on the order of $100\frac{fT}{\sqrt{Hz}}$ in the 1–100 kHz region and this is at least 1,000× more sensitive than the PASCO coils. The new transmitter will have a custom amplifier that can drive 3–4 A of electrical current into a coil with a magnetic core at kilohertz frequencies.

The communication distance depends on the magnetic field (B) generated by the transmitter, the sensitivity of the receiver, and the background magnetic noise. The magnetic field generated at the transmitter is proportional to the INA product, where I is electrical current driving the transmitter coil, N is the number of the loops in the coil, and A is the area of the coil. The PASCO coil has a large number of loops (N = 500), but it has a high inductance (95 mH) and thus, high impedance at high frequencies (e.g., 600 ohms at 1 kHz). So it is difficult to drive a high current into this coil and this limits its INA product. To drive 1 A electrical current into the PASCO coil, we will need an amplifier that can output 600 V root-mean-square or 1.7 kV peak-to-peak, which is unrealistic. To overcome this, we are currently building new coils that can produce higher IN products with realistic amplifier output voltage values.

For MI communication, we are dominated by the $\frac{1}{d^6}$ signal power attenuation factor. Suppose we can increase the transmitter gain by 10× and increase the receiver gain by 1,000× for a total system gain of 10^4. We can then close a communication link that is about 4.6× longer than what we can do now (i.e., $\frac{1}{4.6^6} = 10^{-4}$). Since we have shown a 20 m error-free link for the PASCO coil, our distance limit for an MI communication system that can fit in a cryobot mission would be about 100 m.

To implement an MI communication link in the kilometer range, we will need to generate a much stronger B field. One way to achieve this would be to have a large loop with a very large area at the transmitter. However, this option would not be practical for a cryobot constrained by size, weight, and power. We could also look into the possibility of building an MI waveguide using passive coils. But the spacing between the coils that is required to make this approach work has not been evaluated.

References

[1] D. Wei, et al., "ROV assisted magnetic induction communication field tests in underwater environments," in *Proc. ACM Int. Conf.* WUWNet, Shenzhen, China, pp. 1–5, December 2018.

[2] I. S. Bogie, "Conduction and magnetic signaling in the sea a background review," *Radio Electron. Eng.,* vol. 42, no. 10, pp. 447–452, October 1972.

[3] H. Guo, Z. Sun, and C. Zhou,"Practical design and implementation of metamaterial-enhanced magnetic induction communication," *IEEE Access,* vol. 5, pp. 17213–17229, 2017.

[4] J. J. Sojdehei, P. N. Wrathall, and D. F. Dinn,"Magneto-inductive (MI) communications," in *Proc. MTS/IEEE Oceans,* Honolulu, HI, USA, pp. 513–519, November 2001.

[5] M. Zahn, "Electromagnetic field theory: a problem solving approach," MIT Open Courseware, https://ocw.mit.edu/courses/res-6-002-electromagnetic-field-theory-a-problem-solving-approach-spring-2008/pages/textbook-contents/

[6] J. G. Proakis, M. Salehi, "Digital communications," Fifth Edition, McGraw Hill.

APPENDIX

I. Maximum Likelihood Decision Rule for Non-coherent Detection of OOK

Suppose that for data bit 1, the transmitted signal is

$$s_1(t) = \sqrt{2P}\sin(2\pi f_1 t), \tag{13}$$

where P is the received peak power, and for data bit 0, the transmitted signal is

$$s_0(t) = 0. \tag{14}$$

Then for data bit 1 (hypothesis H_1), the received observation is

$$r(t) = \sqrt{2P}\sin(2\pi f_1 t + \theta) + n(t), \tag{15}$$

where θ is the random phase and $n(t)$ is the received noise. For data bit 0 (hypothesis H_0), the received observation is

$$r(t) = 0 + n(t). \tag{16}$$

Consider the orthonormal basis functions

$$\phi_1(t) = \frac{\sqrt{2}}{\sqrt{T}}\sin(2\pi f_1 t) \tag{17}$$

and

$$\phi_2(t) = \frac{\sqrt{2}}{\sqrt{T}}\cos(2\pi f_1 t), \tag{18}$$

where T is the symbol duration. The inner product between the two basis functions is $\langle \phi_1(t), \phi_2(t) \rangle = \int_0^T \phi_1(t)\phi_2(t)dt = 0$, and the norms of each basis function are

$\langle \phi_1(t), \phi_1(t) \rangle = \int_0^T \phi_1^2(t)dt = 1$ and $\langle \phi_2(t), \phi_2(t) \rangle = \int_0^T \phi_2^2(t)dt = 1$, respectively. The projections of $n(t)$ onto each basis function are $n_1 = \langle n(t), \phi_1(t) \rangle = \int_0^T n(t)\phi_1(t)dt$ and $n_2 = \langle n(t), \phi_2(t) \rangle = \int_0^T n(t)\phi_2(t)dt$. The autocorrelation of white noise $n(t)$ is $R_n(t, \tau) = \frac{N_0}{2}\delta(t - \tau)$. Therefore, n_1 and n_2 are independent with zero mean and each with variance $\sigma^2 = \frac{N_0}{2}$. The components of noise orthogonal to space of $\phi_1(t)$ and $\phi_2(t)$ are irrelevant for detection of signals. After projecting the received waveforms onto $\phi_1(t)$ and $\phi_2(t)$, we get the observation vectors

$$H_1 : \mathbf{y} = \begin{bmatrix} y_1 \\ y_2 \end{bmatrix} = \begin{bmatrix} \sqrt{E}\cos(\theta) \\ \sqrt{E}\sin(\theta) \end{bmatrix} + \begin{bmatrix} n_1 \\ n_2 \end{bmatrix} \tag{19}$$

or

$$H_0 : \mathbf{y} = \begin{bmatrix} y_1 \\ y_2 \end{bmatrix} = \begin{bmatrix} n_1 \\ n_2 \end{bmatrix}. \tag{20}$$

Under hypothesis H_1, the conditional pdf is

$$\begin{aligned} p\left(\mathbf{y}|H_1,\theta\right) &= \frac{1}{\pi N_0} e^{-\frac{1}{N_0}\left[\left(y_1-\sqrt{E}\cos(\theta)\right)^2+\left(y_2-\sqrt{E}\sin(\theta)\right)^2\right]} \\ &= \frac{1}{\pi N_0} e^{-\frac{1}{N_0}\left(y_1^2+y_2^2+E\right)} e^{-\frac{2\sqrt{E}}{N_0}\left(y_1\cos(\theta)+y_2\sin(\theta)\right)}. \end{aligned} \tag{21}$$

Let us consider the following transformation:

$$\begin{aligned} y_1 &= R\cos(\alpha) \\ y_2 &= R\sin(\alpha). \end{aligned} \tag{22}$$

The Jacobian of this transformation is

$$J = \begin{bmatrix} \frac{\partial y_1}{\partial R} & \frac{\partial y_1}{\partial \alpha} \\ \frac{\partial y_2}{\partial R} & \frac{\partial y_2}{\partial \alpha} \end{bmatrix} = \begin{bmatrix} \cos(\alpha) & -R\sin(\alpha) \\ \sin(\alpha) & R\cos(\alpha) \end{bmatrix} \tag{23}$$

with determinant $det(J) = R$, so the conditional pdf $p\left(R,\alpha|H_1,\theta\right)$ is given by

$$p\left(R,\alpha|H_1,\theta\right) = \frac{R}{\pi N_0} e^{-\frac{1}{N_0}\left(R^2+E\right)} e^{-\frac{2\sqrt{E}}{N_0}R\cos(\alpha-\theta)}. \tag{24}$$

Then we have

$$p\left(R|H_1,\theta\right) = \int_0^{2\pi} p\left(R,\alpha|H_1,\theta\right) d\alpha = \frac{2R}{N_0} e^{-\frac{1}{N_0}\left(R^2+E\right)} I_0\left(\frac{2\sqrt{E}}{N_0}R\right). \tag{25}$$

Note that this is independent of θ, and the pdf of θ is $p(\theta) = \frac{1}{2\pi}$ for $0 \le \theta \le 2\pi$. Therefore, we get the Rician distribution

$$p\left(R|H_1\right) = \int_0^{2\pi} p\left(R|H_1,\theta\right) p(\theta) d\theta = \frac{2R}{N_0} e^{-\frac{1}{N_0}\left(R^2+E\right)} I_0\left(\frac{2\sqrt{E}}{N_0}R\right). \tag{26}$$

Similarly, for H_0 we get the Rayleigh distribution

$$p\left(R|H_0\right) = \frac{2R}{N_0} e^{-\frac{1}{N_0}R^2}. \tag{27}$$

The optimum decision rule is to choose H_1 if R satisfies

$$\frac{\frac{2R}{N_0} e^{-\frac{1}{N_0}\left(R^2+E\right)} I_0\left(\frac{2\sqrt{E}}{N_0}R\right)}{\frac{2R}{N_0} e^{-\frac{1}{N_0}R^2}} > 1 \tag{28}$$

or

$$\ln\left(I_0\left(\frac{2\sqrt{E}}{N_0}R\right)\right) > \frac{E}{N_0}. \tag{29}$$

If we define a decision threshold η for R, then we need to solve the following equation for threshold η:

$$\ln\left(I_0\left(\frac{2\sqrt{E}}{N_0}\eta\right)\right) - \frac{E}{N_0} = 0. \tag{30}$$

We can asymptotically approximate $I_0(x)$ as e^x for large x. Using this, the approximate threshold is $\eta_1 = \frac{\sqrt{E}}{2}$, which is similar to the threshold of coherent OOK. The normalized version of this threshold $\zeta_1 = \frac{\eta_1}{\sqrt{N_0 2}}$ will be used in the next section.

The threshold for an envelope detector should also have a bias that is proportional to the variance of noise $\frac{N_0}{2}$. We assume a slight modification of η_1 to arrive at a threshold in the form $\eta_2 = \frac{1}{2}\sqrt{E + \beta\frac{N_0}{2}}$, where β is chosen such that $|\ln\left(I_0\left(\frac{2\sqrt{E}}{N_0}\eta_2\right)\right) - \frac{E}{N_0}|$ is small. For simplicity, the optimization is done over integer values of $\beta \geq 0$. The optimum value of β at very small SNR has been obtained as $\beta = 8$. At a specific higher SNR, β could be as high as 14 for average SNR less than 20dB. Even after checking small deviations from this value, we elected to keep $\beta = 8$. We normalized the threshold $\zeta_2 = \frac{\eta_2}{\sqrt{\frac{N_0}{2}}}$ that will be used in the next section.

II. Performance of Maximum Likelihood Non-coherent Detection of OOK

The probability of error given H_1 using threshold η or the normalized version $\zeta = \frac{\eta}{\sqrt{\frac{N_0}{2}}}$ is

$$\begin{aligned} P(error|H_1) &= P(R < \eta|H_1) = \int_0^{\eta} p(R|H_1)dR = \int_0^{\eta} \frac{2R}{N_0} e^{-\frac{1}{N_0}(R^2+E)} I_0\left(\frac{2\sqrt{E}}{N_0}R\right) dR \\ &= \int_0^{\zeta} \rho e^{-\frac{1}{2}\left(\rho^2+\frac{2E}{N_0}\right)} I_0\left(\sqrt{\frac{2E}{N_0}}\rho\right) d\rho = 1 - Q_1\left(\sqrt{\frac{2E}{N_0}}, \zeta\right). \end{aligned} \tag{31}$$

The pdf of ρ is Rician

$$p(\rho) = \rho e^{-\frac{1}{2}\left(\rho^2+\frac{2E}{N_0}\right)} I_0\left(\sqrt{\frac{2E}{N_0}}\rho\right). \tag{32}$$

For $\sqrt{\frac{2E}{N_0}} > 3$, a metric to determine if the SNR is sufficiently high, it can be approximated with a Gaussian density function

$$p(\rho) \approx \frac{1}{\sqrt{2\pi}} e^{-\frac{1}{2}\left(\rho-\sqrt{\frac{2E}{N_0}}\right)^2}. \tag{33}$$

The probability of error given H_0 using threshold η or its normalized version $\zeta = \frac{\eta}{\sqrt{\frac{N_0}{2}}}$ is

$$\begin{aligned} P(error|H_0) &= P(R > \eta|H_0) = \int_{\eta}^{\infty} p(R|H_o)dR = \int_{\eta}^{\infty} \frac{2R}{N_0} e^{-\frac{1}{N_0}R^2} dR \\ &= \int_{\zeta}^{\infty} \rho e^{-\frac{1}{2}\rho^2} d\rho = e^{-\frac{1}{2}\zeta^2}. \end{aligned} \tag{34}$$

The optimal value of ζ should satisfy that $P(error|H_1)$ is equal to $P(error|H_0)$ for equally likely data bits 0 and 1. The average energy is $\bar{E}$. After replacing E with $2\bar{E}$, we first plotted $P(error|H_1)$ and $P(error|H_0)$ for threshold $\zeta_1 = \sqrt{\frac{E}{2N_0}}$ in Figure 13.

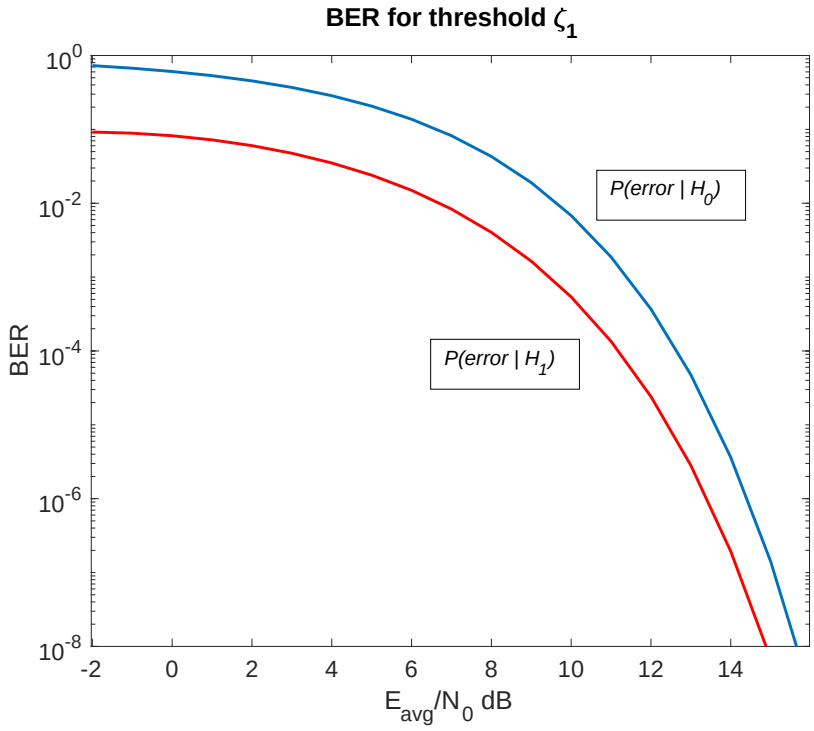

Figure 13. Comparing $P(error|H_1)$ with $P(error|H_0)$ for threshold ζ_1.

Since the curves representing $P(error|H_0)$ and $P(error|H_1)$ do not lie on top of each other in Figure 13, we see that ζ_1 is not close to the optimal threshold. In Figure 14, we instead plot $P(error|H_0)$ and $P(error|H_1)$ with respect to the modified threshold $\zeta_2 = \frac{1}{2}\sqrt{\frac{2\bar{E}}{N_0} + 8}$. We see that the two curves are much closer together, indicating that ζ_2 is a better choice.

As seen from Figure 14, the threshold ζ_2 is a better choice. The average probability of error is $P_e = \frac{1}{2}P(error|H_1) + \frac{1}{2}P(error|H_0)$. Since for $\zeta_2 = \frac{1}{2}\sqrt{\frac{2\bar{E}}{N_0} + 8}$ or $\zeta_2 = \frac{1}{2}\sqrt{\frac{4\bar{E}}{N_0} + 8}$, $P(error|H_1)$ and $P(error|H_0)$ resulted in almost the same performance, we can state that the average probability is

$$P_e = P(error|H_0) = e^{-\frac{1}{2}\zeta^2} = e^{-\frac{1}{2}\frac{\bar{E}}{N_0}-1} = e^{-\frac{1}{4}SNR-1}, \tag{35}$$

where $SNR = \frac{2\bar{E}}{N_0}$.

At this point, we also explore the Gaussian approximation of the Rician distribution

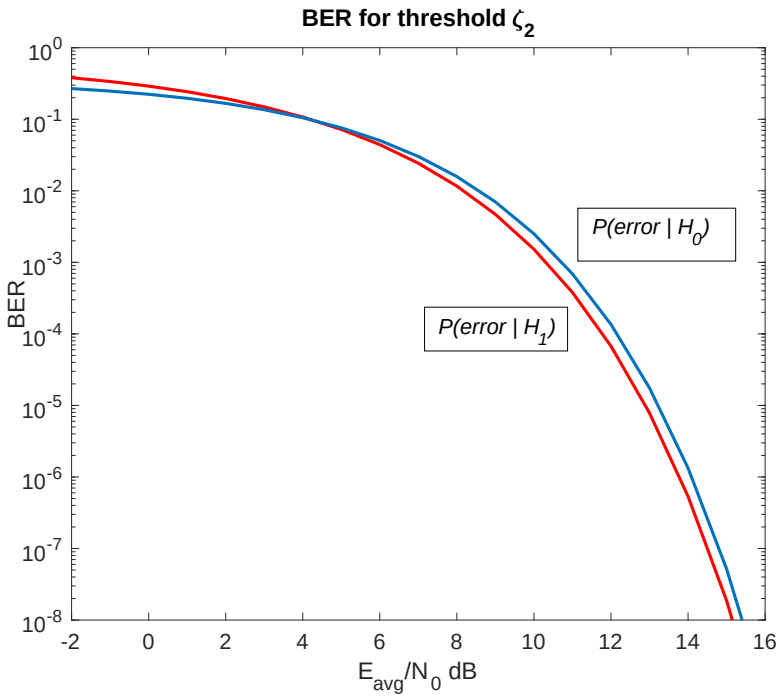

Figure 14. Comparing $P(error|H_1)$ with $P(error|H_0)$ for threshold ζ_2.

to obtain $P(error|H_1)$, using $\zeta_2 = \frac{1}{2}\sqrt{\frac{4\bar{E}}{N_0}+8}$ as follows:

$$\begin{aligned} P(error|H_1) &= \int_0^{\zeta_2} \frac{1}{\sqrt{2\pi}} e^{-\frac{1}{2}\left(\rho-\sqrt{\frac{4\bar{E}}{N_0}}\right)^2} d\rho \\ &= \int_{\sqrt{\frac{4\bar{E}}{N_0}}-\frac{1}{2}\sqrt{\frac{4\bar{E}}{N_0}+8}}^{\sqrt{\frac{4\bar{E}}{N_0}}} \frac{1}{\sqrt{2\pi}} e^{-\frac{1}{2}x^2} dx \\ &= Q\left(\sqrt{\frac{4\bar{E}}{N_0}} - \frac{1}{2}\sqrt{\frac{4\bar{E}}{N_0}+8}\right) - Q\left(\sqrt{\frac{4\bar{E}}{N_0}}\right). \end{aligned} \tag{36}$$

We can ignore the second term, since $Q\left(\sqrt{\frac{4\bar{E}}{N_0}}\right)$ is much smaller than $Q\left(\sqrt{\frac{4\bar{E}}{N_0}} - \frac{1}{2}\sqrt{\frac{4\bar{E}}{N_0}+8}\right)$. Therefore, we obtain

$$P(error|H_1) \approx Q\left(\sqrt{\frac{4\bar{E}}{N_0}} - \frac{1}{2}\sqrt{\frac{4\bar{E}}{N_0}+8}\right). \tag{37}$$

In Figure 15, $P(error|H_1)$ using the Gaussian approximation is compared with $P(error|H_1)$ using the Marcum Q function and $P(error|H_0)$. This figure shows that calculating $P(error|H_1)$ using the Gaussian approximation with ζ_2 is close to the value of $P(error|H_1)$ using the Marcum Q function.

Figure 16 compares $P(error|H_0)$ with average $P_e = \frac{1}{2}P(error|H_1) + \frac{1}{2}P(error|H_1)$

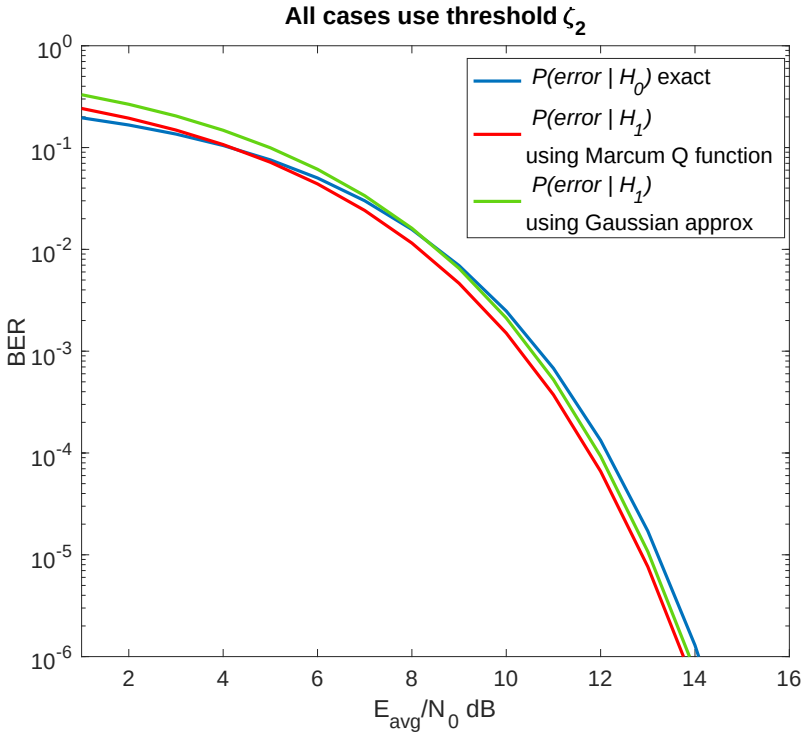

Figure 15. Comparing $P(error|H_1)$ using Gaussian approximation with $P(error|H_0)$.

and verifies that $P(error|H_0)$ is approximately equal to P_e.

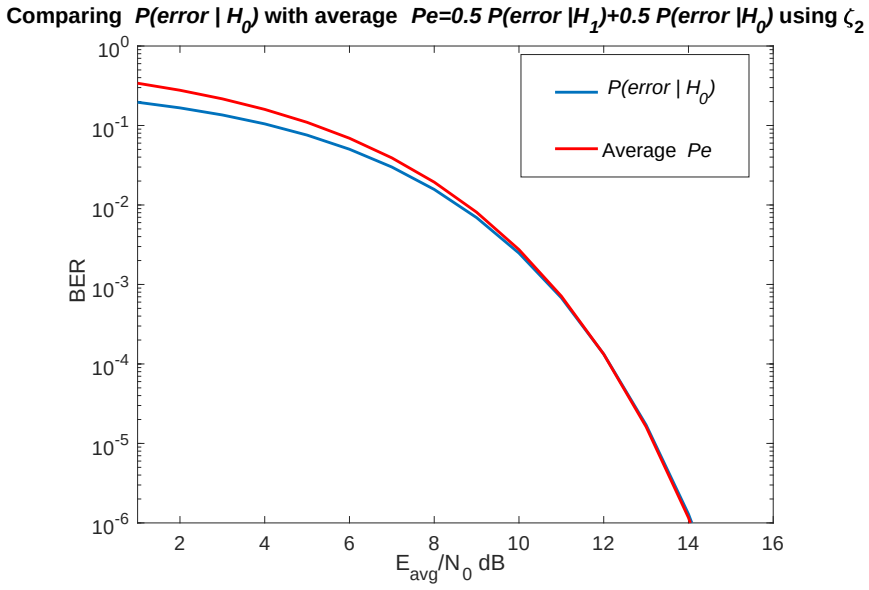

Figure 16. Comparing $P(error|H_0)$ with average Pe.

This shows that we can just use the BER for $P(error|H_0)$, which is an exact closed-form expression but uses approximate threshold ζ_2. We plotted the BER for non-coherent OOK using this equation and compared the performance with the BER of coherent OOK and the BER of coherent binary phase shift keying (BPSK) [6]:

$$P_e = Q\left(\sqrt{\frac{2\bar{E}}{N_0}}\right). \tag{38}$$

Similarly, we plotted the BER for non-coherent OOK against coherent OOK on the same plot. The BER of coherent OOK is as follows [6]:

$$P_e = Q\left(\sqrt{\frac{\bar{E}}{N_0}}\right). \tag{39}$$

The results are plotted in Figure 17.

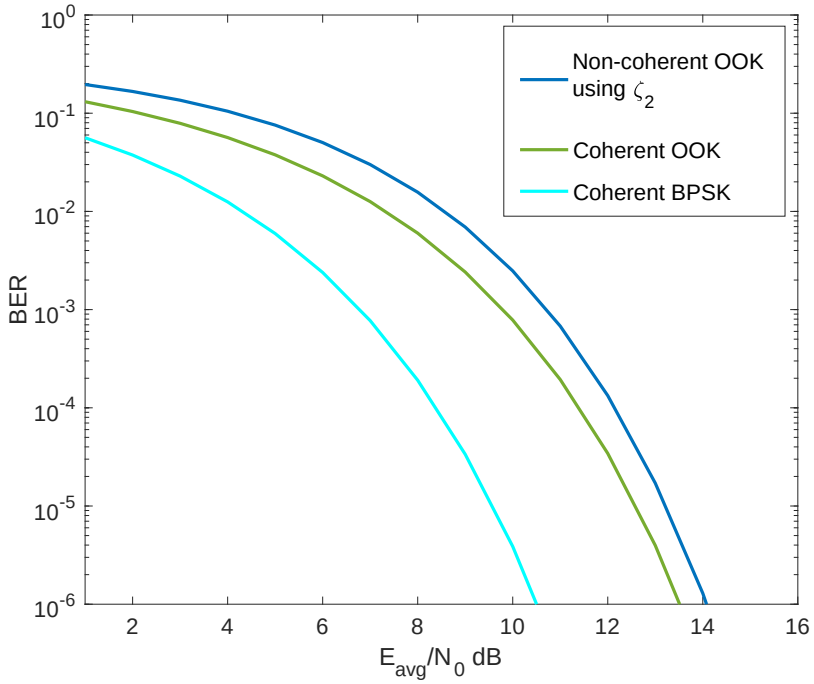

Figure 17. Comparing the BER of non-coherent OOK (using threshold ζ_2 and approximating P_e as $P(error|H_0)$) with the BER of coherent OOK and coherent BPSK.